Pion Electroproduction L-T Separated Cross-Sections at Jefferson Lab

A Prospectus by Jacob Murphy

April 13, 2021

Committee Members
Julie Roche (Advisor)
Martin Mohlenkamp
Daniel Phillips
Zach Meisel

Contents

List of Figures

List of Tables

1 Introduction

The nucleus of the atom consists of neutrons and protons, collectively known as nucleons. Unlike the electrons orbiting the nucleus, nucleons are hadrons: composite objects made up of quarks and gluons. These point-like particles that make up the nucleon are also known as partons[1]. Quarks and gluons are point-like particles that interact with the strong nuclear force. The strong force interaction is mediated through the gluon, the massless boson particle that 'glues' together the quarks. This fundamental force has strength that, except at very short distances, increases with distance between quarks[1]. One consequence of this is quarks are always found in nature bound together and never isolated. Additionally, at short-distance, bound quarks behaves as free particles ignoring each other, with the strong force interaction being weak[2]. This short-distance interaction is the hard physics process, which is calculable through perturbative Quantum Chromodynamics (pQCD). QCD is the strong force theory within the Standard Model of Particle Physics. It describes color charge interaction between quarks via gluons [1]. The Lagrangian of QCD can calculate the hard process via perturbation theory. The soft process, at long-distance interactions, involves significant strong force interactions between quarks and gluons; this is non-perturbative QCD and is not yet well understood.

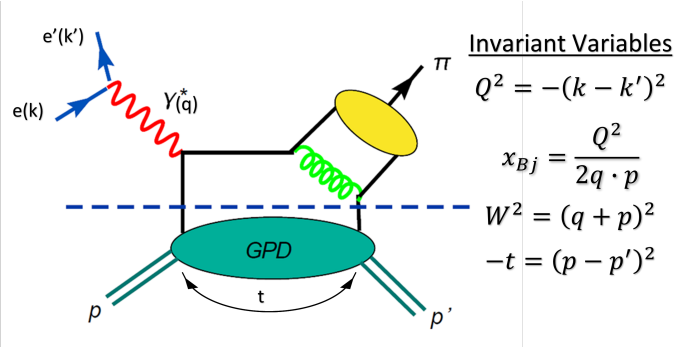

Fig. 1: The handbag diagram for pion electroproduction, taken from [3]. The process above the dashed line is a hard Quantum Electrodynamic (QED) process (left) and a distribution amplitude with a Quantum Chromodynamics (QCD) process (right)[3]. Below the line is a soft QCD process described by GPDs. The quark coupled to the virtual photon γ^* does not interact with quarks below the dashed line in the diagram.

1.1 Internal Structure of the Nucleon

The separation of the short- and long-distance interactions is described by the QCD Factorization Theorem. It calculates high-energy cross-sections with hadrons, adding a scale factor to QCD that separates short- and long-distance parton (quark and gluon) interactions within hadrons[1].

In hadronic physics, there are several parameterization tools to extract the nucleon

long-distance structure. For understanding the spatial distribution of the nucleon constituents (partons), elastic form factors are used. These form factors have been used since the 1950s to study parton spatial distributions. To understand the momentum, Parton Distribution Functions (PDFs) are extracted with Deep Inelastic Scattering (DIS). This tool gives access to the longitudinal momentum of the constituent quarks and gluons[1].

For a more complete picture of the nucleon internal structure, the tool of choice is Generalized Parton Distributions (GPDs)[1]. These functions combine the spatial understanding of the form factors with the momentum distribution extracted from PDFs. GPDs yield a 3-D model of the nucleon and are an invaluable tool in mapping out its structure. They also give insight into the angular momentum and spin structure of the partons[1]. The extraction of GPDs is therefore of vital importance to improve our understanding of nucleons. At Jefferson Lab, one of the major goals of the recent 12 GeV upgrade is the extraction of GPDs[3]. A method of GPD extraction is through meson electroproduction (See Figure 1).

Mesons are hadrons consisting of a quark and anti-quark. The lightest meson is the pion, π. Exclusive pion electroproduction off a proton grants access to the nucleon structure using GPDs. Varying the electron four-momentum transferred squared (Q^2) and the negative nucleon four-momentum transferred (-t) allows for study of the interface between hard (hadronic nucleon) and soft (partonic nucleon) physics. The unpolarized cross-section is defined as

$$\frac{d^2\sigma}{dtd\phi_\pi} = \frac{1}{2\pi}(\frac{d\sigma_T}{dt} + \epsilon\frac{d\sigma_L}{dt} + \sqrt{2\epsilon(1+\epsilon)}\frac{d\sigma_{LT}}{dt}cos\phi_\pi + \epsilon\frac{d\sigma_{TT}}{dt}cos2\phi_\pi) \quad (1)$$

where $\frac{d^2\sigma}{dtd\phi_\pi}$ is the pion electroproduction cross-section. ϕ_π is defined as the angle between the scattering and reaction planes, seen in Figure 2 for π^+ electroproduction. The unpolarized cross-section has contributions from different virtual photon (γ^*) polarizations. The separated cross-sections have γ^* polarizations that are longitudinal (σ_L), transverse (σ_T), have interference between both (σ_{LT}), and have interference between the transverse and itself (σ_{TT}). ϵ is the longitudinal polarization rate of the virtual photon[4].

In pion electroproduction, when -t is equal to the mass of the pion, an isolated pole (the pion pole) exists in the scattering amplitude. At low -t ($-t_{min} < 0.2GeV^2$), σ_L is dominated by the pion pole[5]. The residue of this pole equates to the pion electromagnetic form factor [6]. The pion pole has a distinctive dependence on -t, but also on the longitudinal cross-section, which in combination give access to the pion form factor and the soft physics of the pion[7].

At higher Q^2, approaching the asymptotic limit where Q^2 approaches infinity, the QCD factorization theorem has been rigorously proven for the longitudinal part of the cross-section. This allows for GPD extraction from σ_L. Furthermore, in the asymptotic limit, σ_L is expected to scale with Q^{-6} while σ_T scales to Q^{-8}[3].

The goal of my dissertation research will be to measure the unpolarized cross-section of pion electroproduction in the high Q^2 regime made recently accessible by

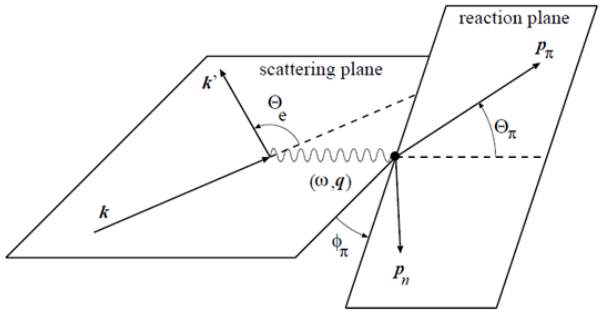

Fig. 2: The kinematics diagram for π^+ electroproduction, taken from [3]. Shown are the in-plane scattering angles θ_e and θ_π for the electron and π^+ meson. The angle ϕ_π is the angle between the plane of electron scattering with the virtual photon exchange, and the plane of the produced hadrons.

the Jefferson Lab 12 GeV upgrade. This will be achieved at Jefferson Lab Hall C under experiment E12-19-006, "Measurement of the Charged Pion Form Factor to High Q2 and Scaling Study of the L-T Separated Pion Electroproduction cross-section at 11 GeV". My dissertation work will result in the measurement of half the data required for the full decomposition of the unpolarized cross-section in terms of its longitudinal and transverse contributions.

1.2 E12-19-006 Experiment

My dissertation research will involve extraction of the longitudinal and transverse cross-sections, σ_L and σ_T, from pion electroproduction. This will be possible through my collaboration with the upcoming experiment E12-19-006: "Measurement of the Charged Pion Form Factor to High Q2 and Study of the L–T Separated Pion Electroproduction cross-section at 11 GeV". The experiment will begin acquiring data August 2021 at Jefferson Lab's Hall C. For convenience and efficient beam-use, this experiment combines two proposals (E12-06-101 and E12-07-105) into one and aims to achieve a measurement of the separated cross-sections along with the measurement of the charged pion form factor; my thesis work, however, will only focus on the former.

The motivation behind this study originates from GPDs, though the extraction of them is not a direct goal. GPD extraction through pion electroproduction relies on precision in σ_L/σ_T separated data[5]. A simple factorization theorem can be applied to longitudinally polarized photons, while a more complicated theorem would be required for the transverse[8]. From this factorization, the short- and long-distance behavior can be separated and allow for GPD extraction from the latter. The factorization theorem is used in the high Q^2 asymptotic limit[5]. In this regime is also assumed that σ_L dominates over σ_T as they scale by factors of Q^{-6} and Q^{-8} respectively[3].

T. Horn and collaborators [9] extracted the separated cross-sections for pion electroproduction for Q^2 up to 3.91 GeV^2. It was found that while σ_L fit well to Q^{-6} scaling, seen in Figure 3, σ_T did not behave as expected (dropping of with Q^{-8}). At the larger Q^2 σ_T was shown to in fact be larger than σ_L.

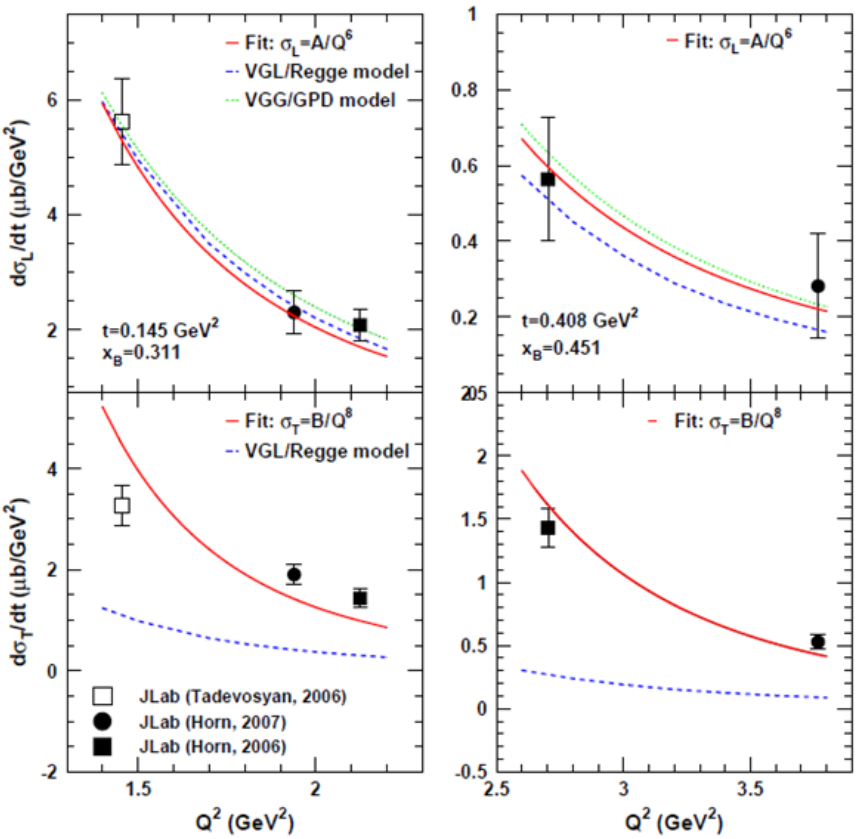

Fig. 3: The L-T separated cross-sections as a function of Q^2, taken from [3]. The solid red line shows a fit of the form Q^{-6} for σ_L and Q^{-8} for σ_T. The dotted green line is from a GPD calculation. The dashed blue lines is a VGL/Regge Model calculation. σ_T was found to be consistently under predicted by the Regge model, which the -t dependence of the cross-section is found by the exchange of Regge trajectories (family of resonances for bound states[10]) with pion-like particles[9].

To follow up on these results, the upcoming pion electroproduction experiment will extract the separated cross-sections at high precision as well as high values of -t and Q^2. More specifically, the separated cross-sections will be found for the reaction $p(e, e'\pi^+)n$ using a liquid hydrogen target. The measurable result of this experiment will be separated cross-sections up to $Q^2 = 8.50$ GeV^2, varying -t, and $x_{Bj} = 0.3$, 0.4, 0.55, where x_Bj is the Bjorken-x variable defined as the momentum fraction (see Figure 1 for definition).

The longitudinal and transverse cross-sections will be separated using the Rosenbluth Separation. This will involve data collection at two values of ϵ with the invariant

mass (W), Q^2, and -t held constant along with a simultaneous fit using the azimuthal angle (ϕ_π). To this effect, if $\sigma_1 = \sigma_T + \epsilon_1\sigma_L$ and $\sigma_2 = \sigma_T + \epsilon_2\sigma_L$, then

$$\sigma_L = \frac{1}{\epsilon_1 - \epsilon_2}(\sigma_1 - \sigma_2) \tag{2}$$

will allow for determining the separated cross-sections[3].

To access the beam energies required for this experiment, data collection has been divided into three parts. First, a low beam energy (E_e) set of kinematics was collected in the summer of 2019, with $E_e = 2.8, 3.7, 4.6$ GeV. The second part will run Autumn 2021 with $E_e = 6.6, 8.0, 9.2, 9.9$ GeV. The third and last part of the kinematics will need to be collected in 2022 or later, with $E_e = 11$ GeV.

Q^2	W	x_{Bj}	$-t_{min}$	Run Type	E_e	ϵ	θ_{HMS}	θ_{SHMS}	Hrs
3.85	3.07	0.311	0.120	LH+	8.0	0.301	34.15	5.50, 6.53, 8.53	33.5
					9.9	0.572	19.78	7.31, 9.31, 11.31	13.3
5.00	2.95	0.390	0.209	LH+	8.0	0.238	42.91	6.35, 8.35	74.5
					9.9	0.530	23.41	7.76, 9.76, 11.76	41.1
6.00	3.19	0.392	0.214	LH+	9.2	0.184	46.43	5.50, 7.13	182.2
					9.9	0.304	34.23	6.64, 8.64	80.6
3.85	2.02	0.546	0.487	LH+	6.0	0.582	31.02	13.58, 15.58, 17.58	9.6
6.00	2.40	0.551	0.530	LH+	8.0	0.449	33.92	9.26, 11.26, 13.26	48.5
8.5	2.79	0.522	0.550	LH+	9.2	0.156	57.70	5.52	388

Tab. 1: Table of planned 2021 kinematics used to study Pion L-T separated cross-sections beginning in August 2021. There are between 2 and 4 planned kinematics with different ϵ values for a given set of Q^2, W, x_{Bj}, and $-t_{min}$. Only the 2021 kinematics are shown here.

This pion electroproduction experiment will be completed at Jefferson Lab, in Newport News Virginia, using the Continuous Electron Beam Accelerator Facility (CEBAF). CEBAF accelerates electrons through two superconducting linear accelerators [11]. The polarized electron beam originates from a load-locked gun with a photocathode consisting of thin, alternating layers of GaAs and GaAsP. This beam is sent with a current of up to 180 μA [12] to each of the four beam halls: A, B, C, and D. Halls A, B, and C each have access to the beam accelerated up to 5 passes through both linear accelerators, with Hall D having access to half a pass more [12]. At present, a maximum beam energy of 12 GeV can be reached with CEBAF.

In Hall C of Jefferson Lab, there are two spectrometers available for particle detection: The High Momentum Spectrometer (HMS) and Super High Momentum Spectrometer (SHMS), seen in Figure 4. Spectrometers accept charged particles within a narrow momentum and trajectory window. Charged particles that enter the narrow window of the spectrometer's collimator then pass through a magnetic field curving the trajectory proportional to the particle momentum. In the counting house for Hall C, users can adjust the angles of both spectrometers relative to the beamline. Due to the size of the spectrometers, there are restrictions to the angles attainable, with an

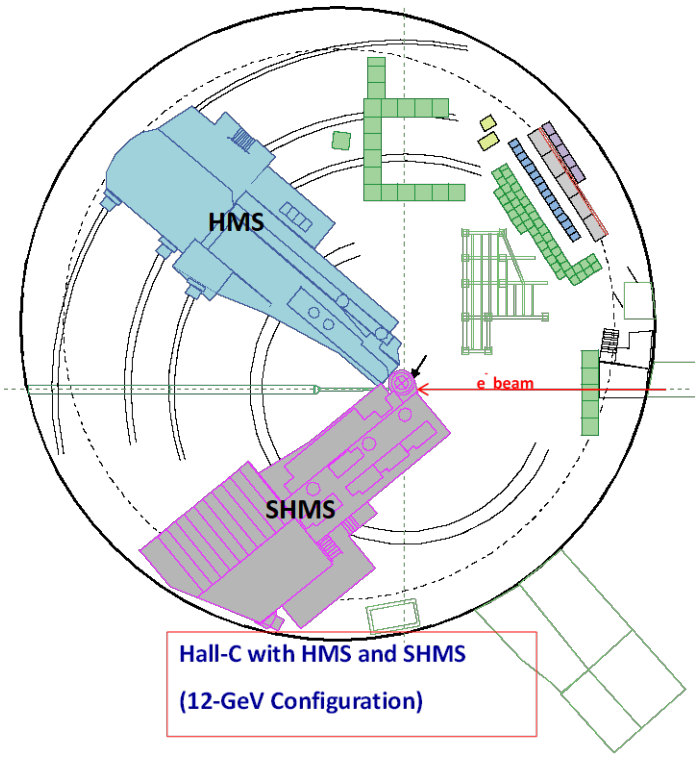

Fig. 4: Top-down diagram of Hall C beam hall with the HMS and SHMS detectors, taken from [13]

SHMS angle range of 5.5 to 40° and an HMS angle range of 10.5 to 85°. Additionally, a minimum opening angle of 17.5° must be kept between the HMS and SHMS to avoid a collision between the two detectors. The SHMS can be set to central momentum values between 2 and 11 GeV/c with a -10% to +22% acceptance; the HMS can set to central momentum values from 1 to 7.3 GeV/c with an acceptance of -9% and +9%[14].

Both spectrometers contain an attached detector stack that particles curve up into after they pass through the generated magnetic field (see Figure 9). Included in these detector stacks are drift chambers, scintillator hodoscopes, threshold Cerenkov detectors, and electromagnetic calorimeters. The drift chambers consist of layers of anode and cathode wire planes with argon-ethane gas; they are used to track the position and angle of particles leaving the magnetic field. Electron showers created in the gas, allow for the trajectory tracking. Hodoscope planes are arrays of scintillators, which emit light when a particle passes through; these planes are used for particle triggering, detection, and tracking. Cerenkov particle detectors utilize the Cerenkov radiation - a cone of light emitted when particles move faster than the speed of light in a medium. Threshold Cerenkov detectors are filled with a specified medium that triggers the radiation cone at a threshold velocity. With the spectrometer determining particle momentum, the mass of the particle is identified based on if the light cone is produced. Finally, EM calorimeters absorb the charged particle, creating a 'shower'

of photons as the particle is slowed down and emits this radiation. In this way, the energy of the particle is absorbed into the calorimeter and is used for particle identification [15].

Our kinematics for the 2021 run, seen in Table 1, will use two 10 cm target cells of liquid hydrogen (LH) and liquid deuterium (LD). For half of the LD and all of the LH kinematics, the HMS will be set to a negative polarity and will collect the scattered electron while the SHMS will be set to a positive polarity and collect the emitted π^+. For the other half of the LD runs, the SHMS will be set to a negative polarity and collect π^-. The emitted nucleon (neutron for π^+, proton for $\pi-$) will be collected from the measured from the missing mass of the reactions. For a given set of W, Q^2, and -t values, there are at least two beam energy values set to be (or have been) collected. W, Q^2, and -t are held constant by adjusting the angle and momenta of the spectrometers.

2 Completed Work

I joined Dr. Roche's research group in the summer of 2019 after the completion of my first year core courses. This section reviews my work completed so far with Dr. Roche, divided into three research projects.

2.1 Elastic Calibration

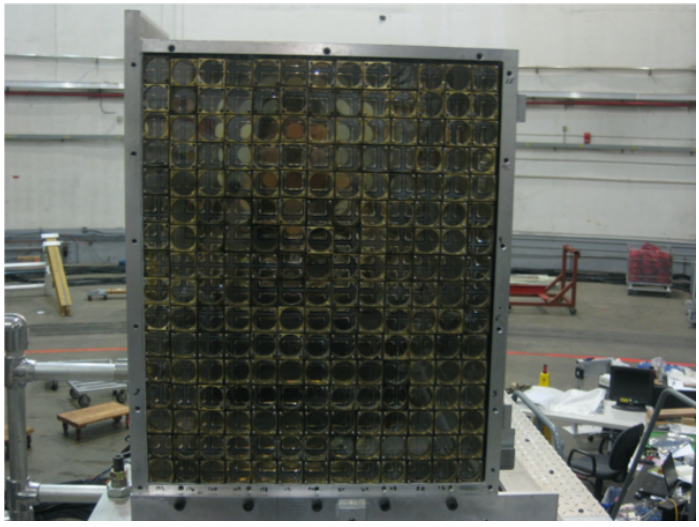

Fig. 5: The calorimeter used in the DVCS in Hall A collaboration. Seen here is the face of the calorimeter with 13 by 16 lead-tungsten blocks inside brass support frames with circular openings. Behind each block is a photo-multiplier tube (PMT) that converts the EM shower to a digital signal via Flash Analog-to-Digital Converter(FADC).

An important step in data collection is calibration runs. When working with

magnetic spectrometers, offsets in the detector angles or central momentum values must be very well-understood to allow for high-precision kinematic reconstructions. A useful type of calibration involves elastic scattering. In elastic scattering of an electron off a proton, the kinematics are over-determined; only two of the following are required: the beam energy, scattered electron momentum, recoil proton momentum, scattered electron angle, and recoil proton angle. Using two well-known measured values (e.g. beam energy and scattered electron angle), the other kinematics variables can be reconstructed (eg. electron momentum, proton momentum, and proton scattering angle) and compared to the measured values.

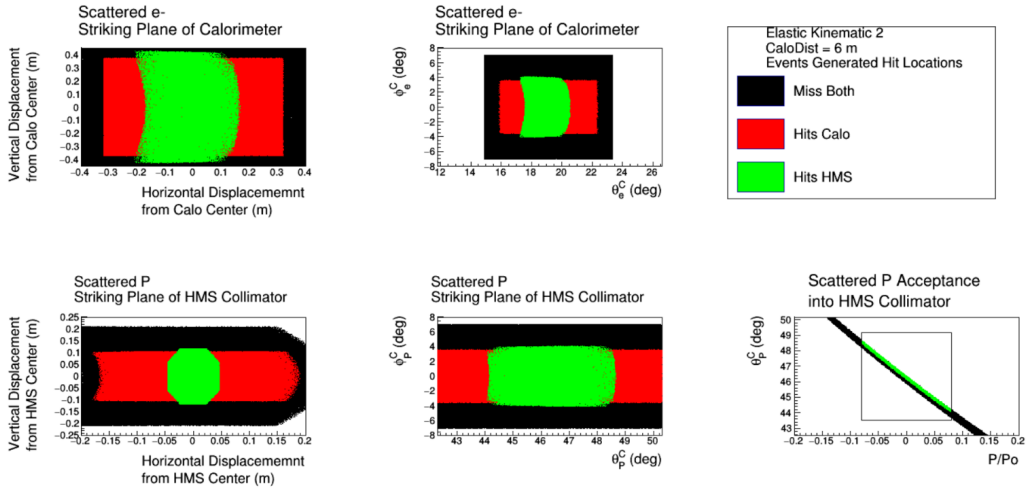

Fig. 6: Results of the simulation for the first kinematic in Table 2, at a calorimeter distance of 6 meters from the pivot point. The first subfigure shows electrons striking the plane of the face of the calorimeter. Similarly, the fourth shows where protons strike the plane of the collimator of the HMS. The second and fifth subfigures show the same results but with electron and proton angles (Cartesian). The sixth subfigure shows the limitations of the HMS acceptance, with the X-axis being normalized momentum and the y-axis being incoming θ_P angle.

Elastic calibration runs are planned for the upcoming Pion-LT experiment. Due to delays in the beam hall schedule, my dissertation research topic switched to the Pion-LT experiment from Deep Virtual Compton Scattering (DVCS) with the Neutral Particle Spectrometer (NPS). Prior to this change, I developed a simulation for elastic calibrations for the NPS experiment. The results and recommendations from this simulation were presented and submitted to the collaboration in the report in Appendix A. NPS is planned to run in Hall C of Jefferson lab, using the HMS detector. One significant difference between these two experiments is that for NPS the SHMS is not used and is replaced with the NPS calorimeter. The calorimeter for the 2016 DVCS experiment in Hall A of Jefferson Lab is shown in Figure 5; it is similar in design but the NPS calorimeter will be larger. While the spectrometers require calibration of angle and central momentum, the NPS calorimeter requires en-

ergy calibrations for each lead tungsten cell of the detector. For the calorimeter, a particle striking a cell will result in an FADC (Flash Analog to Digital Converter) reading proportional to its energy. Each cell is in parallel and consequentially requires independent calibration.

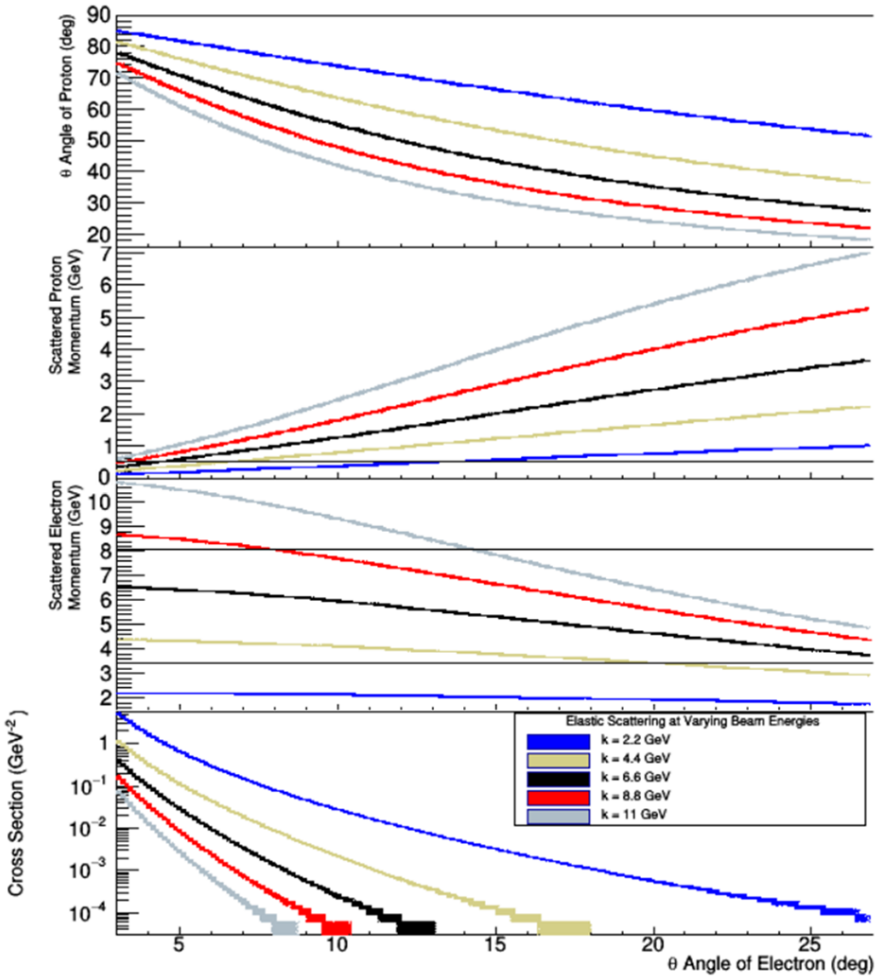

Fig. 7: From top to bottom: scattered proton angle, scattered proton momentum, scattered electron momentum, and elastic cross-section as a function of electron scattering angle. The different colored lines indicate energy of the incident electron beam. Horizontal black lines show detector limits for HMS (proton) or desired kinematic range for the calorimeter (electron).

The planned method for this calibration is to use elastic scattering in coincidence, where both the scattered electron and recoil proton are detected for a given scattering event. With the proton momentum measured by the HMS and beam energy known, the momentum of a coincidence electron striking the calorimeter is determined independently of the FADC. To calibrate each cell of the calorimeter while minimizing calibration time, the acceptance of elastic coincidence must cover the entire face of the calorimeter. This was the specific motivation for creating such a simulation- de-

termining what coincidence kinematics would be required to calibrate each cell of the NPS calorimeter.

In the elastic calibration for NPS, the electron will be detected by the calorimeter with the proton collected into the HMS. The target is liquid hydrogen (LH2) with a length of 10 cm. The spectrometer distance from the pivot point is fixed, but the NPS calorimeter distance will be variable. Knowing the detector entrance dimensions, and momentum acceptance of the HMS (see Appendix A for specifics), a simulation was then generated. Inputs to the simulation were determined from the planned kinematics of the NPS DVCS experiment. One goal of the elastic calibrations is to calibrate the calorimeter for momenta values close to those expected in the DVCS experiment.

Variable	Units	Kin1	Kin2	Kin3
k	GeV	4.4	6.6	8.8
k'	GeV	3.5	5.5	7.5
θ_e	deg	19.1	13.7	11
P	GeV	1.58	1.81	2.03
θ_P	deg	46.3	46	44.9
Rate	Events/sec	87	64	45
Rate per Block	$\times 10^{-2}$ Events/sec	24	25	22
Time to 1000 Events per Block	hrs	1.2	1.1	1.3
% Calorimeter in Coincidence	%	30	21	17

Tab. 2: Proposed Elastic Kinematics for NPS DVCS calibration, maximizing cross-section while restricted by experimental bounds. Rate is calculated for 1 μA beam current.

It was found that an acceptance could be generated covering the entire face of the calorimeter for the desired kinematics for elastic calibration. However, this acceptance was only achievable by moving the calorimeter back to a distance of 11 m from the pivot point. As a consequence, the event rate for these kinematics was too low for calibration. Coincidence event rates dropped dramatically as the distance between the target and calorimeter increased. In the other extreme, at distances below approximately 6 meters between the target and calorimeter, the acceptance dropped sufficiently to not cover the vertical extension of the calorimeter face. This is seen in Figure 6, where the events hitting the calorimeter (red) overlap with the events hitting the HMS (green). At smaller acceptance (with higher rates), multiple angle settings could be applied to sweep the calorimeter face horizontally. The only method to include the vertical extremes of the calorimeter is to increase the acceptance by placing the calorimeter further back. As a result, the calibration distance between the pivot and calorimeter was determined at 6 m. To compensate for the lower rate of events, kinematics had to be chosen to increase the elastic cross-section.

Seen in Figure 7, the elastic cross-section quickly drops as electron scattering angle increases. Here the elastic cross-section is calculated using the product of the Mott cross-section and the Dipole form factors. A decrease in beam energy is shown to have a much larger cross-section, resulting in a higher rate. As a result of the limitations

in the detectors and requirements for calibrating the calorimeter, I proposed three elastic kinematics for calibrating the NPS calorimeter in the NPS DVCS experiment, seen in Table 2.

2.2 Machine Learning Project

In working with the DVCS in Hall A collaboration, my research included the exploration of the value of a machine learning algorithm using calorimeter data. The analysis of the calorimeter signals is currently the slowest step in data processing. These data were from the DVCS III experiment in Hall A of Jefferson Lab. In that experiment, when a particle such as a photon strikes the calorimeter, a shower of photons cascades through it. The energy from this shower is converted to some voltage that is recorded once every nanosecond (ns) for a duration of 128 ns. The calorimeter consists of an array of lead-glass blocks, see Figure 5. When a block is struck by a high-energy photon from a scattering event, a peak in the voltage signal is produced, with a characteristic shape. The shower produced by a photon striking a calorimeter block spreads to adjacent blocks, resulting in the incident photon energy spreading across several cells. Because of the shower spread, the amplitude of the peaks in every calorimeter cell are necessary to reconstruct the momentum of the scattered particle. An additional problem arises when, typically at higher event rates, two photons strike the calorimeter within the recorded time window of 128 ns. The voltages are recorded if a coincidence event is detected, but only one photon within the time window will correspond to the scattering event. If the second photon additionally strikes a block close to the originally struck block, a two-peak signal will be recorded.

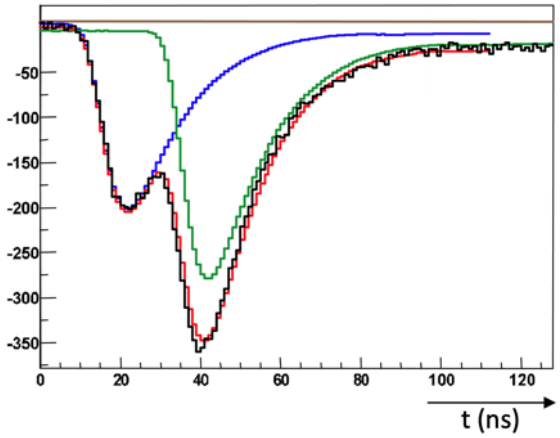

Fig. 8: Two-pulse signal shape of FADC calorimeter signal from DVCS III calorimeter. Plotted is the data signal (black), the fitted 2-pulse signal (red), the two individual signals (blue and green), and the linear baseline.

The FADC signal from the blocks of the calorimeter will consequently have 3 forms: either two, one, or a no-pulse signal. This is demonstrated in Figure 8, where the data signal is in black. The present method of analysis performs a χ^2 fit of a

baseline (no-pulse) signal, see the top line in Figure 8. If the resulting fit has a χ^2 larger than the threshold value, a second fit is performed. The second fit takes a predefined pulse shape and attempts to match it to the data at any given time or amplitude, similar to the blue and green pulses in Figure 8. If again a threshold minimization value is not reached, a third fit is performed, similar to the first but fitting a 2-pulse shape; this is the red signal in Figure 8. As the photons have a well-defined voltage signal, this method has worked well, though the analysis is slow.

At Jefferson Lab, I met with members of the Machine Learning Lunch group to discuss this DVCS problem. Per their suggestion, I submitted the problem to the group as a part of their 'Problem of the Quarter'. To facilitate this, I communicated a detailed description of the problem (see Appendix B). I then organized a training data set, containing the input 128-signal arrays and the desired output values. These values were the two amplitudes and times of the pulses found using the χ^2 method currently used by the DVCS group. For events without a second or first pulse, I set amplitudes to 0 and times to -1. The training set and problem write-up were given to the ML Lunch group at Jefferson Lab, with 3 months to complete the problem. I additionally gave a presentation on the material and answered questions regarding the data set during this 3 month period. At the end of the quarter, I developed and sent out a test data set, containing the 128-signal arrays only. Participants returned their solution codes and results, which I graded to the results from the χ^2 method. Solutions were judged on their pulse times and amplitudes (two per event, null or otherwise), along with number of recorded pulses (0, 1, or 2). Using the χ^2 method as an answer key, the sum differences squared were taken for each category.

Three different machine learning algorithms were submitted, with varying degrees of success. The winning code had the best score (lowest sum) in each category. Using the python package Tensorflow 2, the winners used a neural network with a custom activation function for the null-pulse values. This code was saved to be potentially implemented in the upcoming NPS DVCS experiment. In the discussion of the machine learning programs development with the candidates, each noted issues with the provided training data. The χ^2 method had been mislabeling events, causing significant issues to the ML process. Approximately 1% of the data selected had events labeled as "no-pulse" when two pulses were clearly visible. Additionally, there were some two-pulse events that were simply noise. To use the data for ML training, it required significant clean-up from the candidates and consequentially revealed issues with the current method of pulse-fitting used by the DVCS III experiment group.

2.3 Hall C HMS Saturation Corrections

For the upcoming pion electroproduction experiment in Hall C of Jefferson Lab, the detectors used in particle detection are both spectrometers. The High Momentum Spectrometer (HMS) will be used to measure scattered electrons. A spectrometer such as the HMS is a useful device for measuring scattered particles because it has two acceptance restrictions. First, there is an angular acceptance window on the

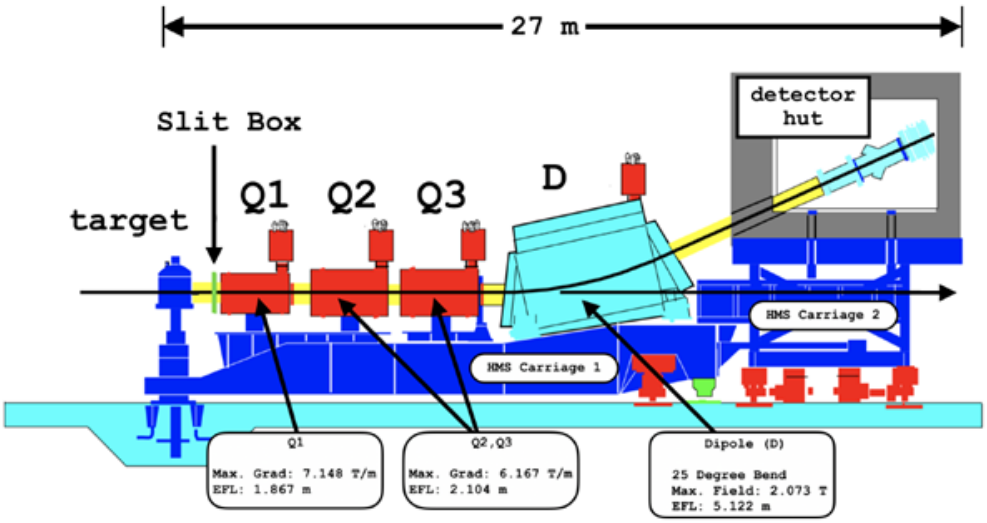

Fig. 9: Side-view of the High Momentum Spectrometer in Hall C of Jefferson Lab, taken from [15]. The dipole and three quadrupole magnets (D, Q1, Q2, Q3) generate a magnetic field that curves charged particles (of central momentum p_0) into the shielded detector hut.

device from the placement of the detector, the target, and the opening of the spectrometer. For any given experiment in Hall C, the HMS distance to the pivot (point at which the target cell is centered) is fixed. The spectrometer can be rotated, allowing for different regions of angular acceptance. If a particle is within this window, it will enter the collimator of the HMS into the spectrometer itself. A spectrometer contains a magnetic field that will curve the trajectory of charged particles. The HMS achieves this magnetic field through a dipole and three quadrupole electromagnets, seen in Figure 9. The magnets are fed some amount of current to generate the desired magnetic field strength within the spectrometer. Just as a user would set the spectrometer angle, they also set the field strength by adjusting the current in the electromagnets. The field strength is set to allow particles of a central momentum (p_0) value to pass through the center of the detector. The HMS can have a p_0 value from 0.5 to 7.5 GeV/c and only particles with momentum within a resolution range around p_0 will be accepted through the spectrometer.

After a particle is accepted into the HMS and it passes through the magnetic field, the particle trajectory passes through a non-real focal plane. This focal plane intersection allows for the extraction of the physical properties from the scattered particle. In the focal plane, a particle's dispersive position (x_{fp}) and angle (x'_{fp}) as well as its transverse position (y_{fp}) and angle (y'_{fp}) are measured by the wire chamber. The trajectory of the particle before the magnetic field and its momentum are reconstructed. This is accomplished through the Optical Matrix of the HMS - a matrix of coefficients used to compute the vertical scattering angle (x'_{tar}), the horizontal scattering position (y_{tar}), the horizontal scattering angle (y'_{tar}), and the particle momentum fraction relative to the HMS central momentum (δ). The equation

$$\begin{bmatrix} x'_{tar} \\ y_{tar} \\ y'_{tar} \\ \delta \end{bmatrix} = M \begin{bmatrix} x_{fp} \\ x'_{fp} \\ y_{fp} \\ y'_{fp} \end{bmatrix}, \tag{3}$$

where M is the Optical Matrix, defines the relationship between the focal plane and physics variables. The matrix elements are coefficients used to reconstruct the physics variables from the focal plane elements. For example, one matrix column has elements that are coefficients C for reconstructing x'_{tar} through:

$$x'_{tar} = \sum_{i,j,k,m=0}^{6} C_{ijkmn}(x_{fp})^i(x'_{fp})^j(y_{fp})^k(y'_{fp})^m \tag{4}$$

where the focal plane variables are used up to 6th order with the coefficients of the optical matrix.

The HMS is named as such due to its capacity to detect scattered particles at momenta up to 7.5 GeV/c, though until recently the beam energy only went as high as 5.5 GeV. In the 12 GeV era of Jefferson Lab, this capacity can be used to great advantage in accessing a number of high-energy kinematics. However, an issue was discovered with this detector after the 12 GeV upgrade. When set to collect particles of momenta greater than 5 GeV/c, the magnets of the spectrometer begin to saturate. The linear relationship of current-to-field-strength begins to drop off at these extreme settings. As a result of this, for p_0 values set above 5 GeV/c, a known current into the electromagnets does not equate to a well-understood magnetic field strength or central momentum value.

The saturation effects cause issues with the reconstruction of the non-central trajectories. To compensate for the saturation effects, the optical matrix needs to be re-determined for higher p_0 settings. In order to determine such coefficients, calibration runs must be used where the physics variables (x'_{tar}, y_{tar}, y'_{tar}, δ) are known along with the focal plane variables.

The optical matrix calibration is completed in two parts: a calibration for scattering angle/position using Carbon-Sieve optics followed by momentum calibration using elastic hydrogen data.

2.3.1 Carbon-Sieve Optics

First, the new x'_{tar}, y_{tar}, and y'_{tar} matrix coefficients are calculated. To find the scattering angle and target position without the optical matrix, two calibration measures were implemented. First, electrons scattering off a carbon foils target was chosen for calibration. The benefit of this target is in its dimensions, as it is thin enough to be considered 2D. As a result, the scattering position along the beamline is very well-defined for any given event; this is determined via graphical cuts as seen in Figure 10. The second calibration measure was the use of a sieve slit. The sieve slit is a thick metal sheet with holes, which is placed in front of the spectrometer. The well-known

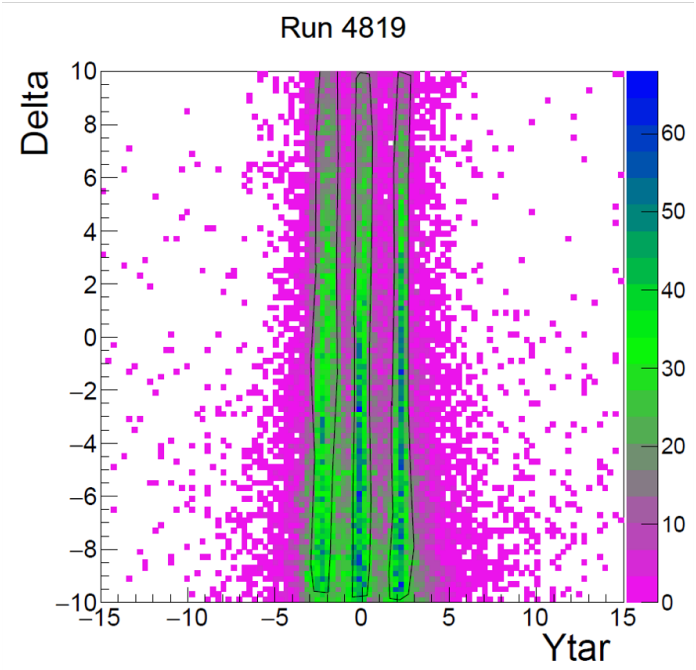

Fig. 10: 2D histogram of δ as a function of Y_{tar}. The black outlines around the green data region show the graphical cut placed on the data. This histogram shows the three target carbon foils scattered off of for these events in run 4819. The graphical cuts allow the target foil to be selected, giving a known target scattering position of 10,0 or -10 cm in the beamline (with respect to the pivot point).

pattern and spread of the holes in the sieve slit is reflected in the focal plane of the spectrometer, see Figure 11, as only scattered particles passing through the holes may enter. Knowing the sieve hole entrance of a scattered particle, in combination with the target carbon foil scattering position, allows for the scattering trajectory to be reconstructed. With the detector position and orientation relative to the pivot well-known as well, the scattering angles and target position were reconstructed for the scattered electrons passing through the sieve holes. Finally, a minimization calculation was applied to the difference between the matrix reconstructed variables (using equations like Equation 4) and the values determined from the carbon foil sieve slit optics. To minimize this difference, the matrix coefficients were adjusted until a solution was found. The result of this process was a partially corrected optical matrix, with the x'_{tar}, y_{tar}, and y'_{tar} coefficients corrected to accurately reconstruct their respective physical values.

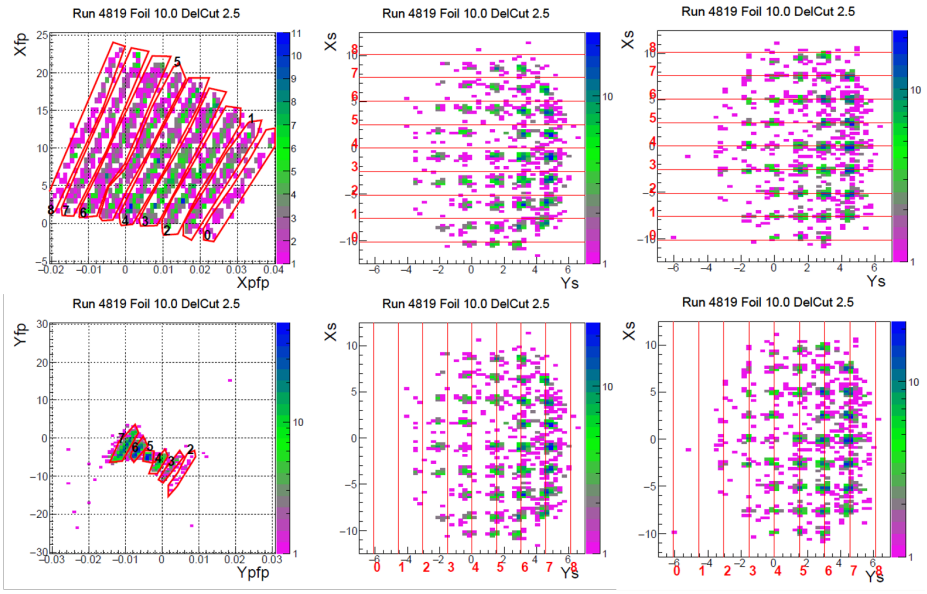

Fig. 11: Focal plane events taken from run 4819 of the Kaon-LT experiment. Data cut from one carbon foil within a delta region about +2.5%.

2.3.2 LH2 Elastic Delta Scan

The second part of the optics calibrations corrects the δ coefficients in the optical matrix. δ is the fractional momentum defined as

$$\delta = \frac{p_0 - P}{p_0} \times 100 \tag{5}$$

where p_0 is again the central momentum of the HMS and P is the collected particle momentum. To reconstruct δ without the optical matrix, elastic scattering off of a liquid hydrogen (LH2) target was used. When an electron scatters elastically off a proton, the squared invariant mass of the system, W^2, is the mass of the proton squared, M_P^2. Using the definitions

$$W^2 = M_P^2 + Q^2(\frac{1}{x_{Bj}} - 1) \tag{6}$$

$$Q^2 = 4E_0E'\sin^2(\theta/2) \tag{7}$$

$$x_{Bj} = \frac{Q^2}{2M_P(E_0 - E')} \tag{8}$$

and the invariant mass under elastic scattering ($W^2 = M_P^2$), the elastically-scattered electron momentum (E') can be defined in terms of the scattering angle (θ), the incident beam energy (E_0), and M_P. This allows for δ to be defined with minimal

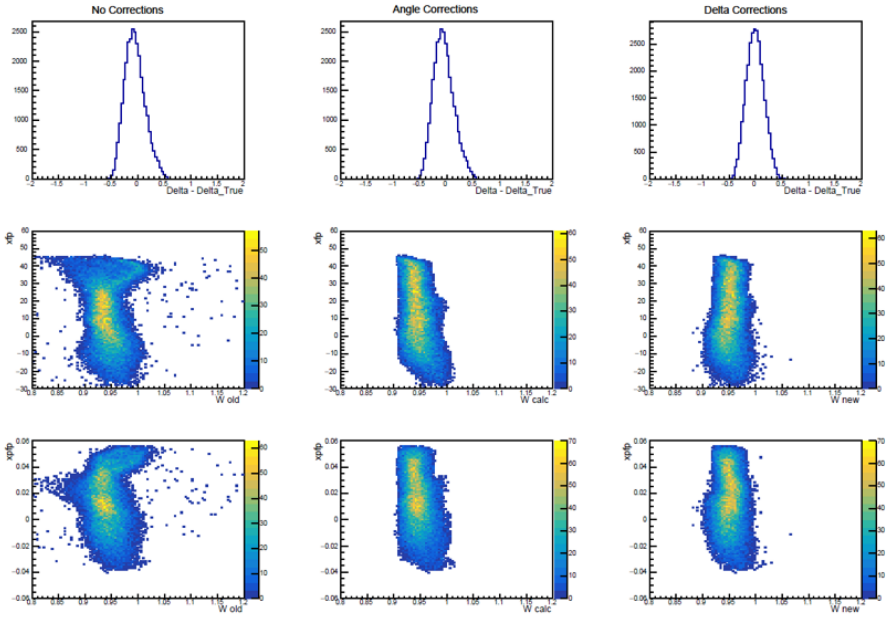

Fig. 12: Graphical cut of x_{fp} and x'_{fp} versus W. The top row of 1-D histograms shows the difference in delta from the optical matrix and the true value. The second and third row 2-D histograms are x_{fp} and x'_{fp} versus W. From left to right the columns show these results with the original matrix, the matrix after carbon-sieve optics calibrations, and the matrix after all calibrations. The events shown are across nine data runs, and were previously cut using the middle column data.

usage of HMS quantities. It is assumed that p_0 is well-known and that θ has been corrected from the carbon-sieve optics calibrations.

Elastic scattering events were selected based on W in the focal plane. Graphical cuts were places at the events near $W = M_P$ in x_{fp} and x'_{fp}. In Figure 12, the results of the graphical cut are seen in the lower middle-two subfigures, where only the events within the cut shape remain. Events were selected across nine data runs that scanned δ and maximized focal-plane coverage. δ was then calculated from θ, E_0, and M_P. The difference was minimized between this δ value and the one determined by the HMS optical matrix. Corrections were applied to the δ coefficients of the optical matrix to solve for the minimization, equivalent to the method used in the scattering angle and position corrections. As a result of these two calibration corrections, a new optical matrix has been developed for use with the HMS at a central momentum of 6.59 GeV/c. This matrix is being made available to Hall C users and currently is being applied to experimental data from the Kaon-LT runs from the fall of 2018.

3 Future Plans

As of the conclusion of the Spring 2021 Semester, I will have completed six core courses and six beyond-core courses, fulfilling the departmental requirement.

My involvement with the upcoming experiment E12-19-006 will include taking shifts on-site as well as being on call for potential issues users may have while running the experiment during this four-month period (see Table 3). In preparation for this, I am familiarizing myself with Hall C analysis techniques using HCANA (Hall C Analyzer) while also working on offline and online analysis scripts. Currently, I am also calculating and selecting potential elastic kinematics for calibration of the HMS and SHMS. After the 2021 data collection run, I will begin my analysis to extract the pion electroproduction cross-section. Extraction of the L-T separated cross-section will be limited as this data run will not include the high-ϵ kinematics needed for Rosenbluth separation. Phase 3 of this experiment, the high-ϵ kinematics, may be included in my dissertation work if scheduling allows. The extent of my involvement with that data run will depend on my analysis progress from the 2021 data.

E12-19-006 Low-ϵ Data Taking Begins	August 2021
E12-19-006 Low-ϵ Data Taking Ends	December 2021
E12-19-006 High-ϵ Data Taking Begins	August 2022
E12-19-006 High-ϵ Data Taking Ends	October 2022
Expected Graduation Date	May 2024

Tab. 3: Expected dates for the Pion Electroproduction experiment E-12-19-006 data collection and graduation.

References

1. T. W. Donnelly, J. A. Formaggio, B. R. Holstein, R. G. Milner, and B. Surrow, *Foundations of nuclear and particle physics* (Cambridge University Press, 2017).

2. A. Belitsky and A. Radyushkin, Physics Reports **418**, 1–387 (2005).

3. T. Horn, G. M. Huber, *et al.*, *Scaling Study of the L-T Separated Pion Electroproduction Cross Section at 11 GeV*, Tech. Rep. (Jefferson Lab PAC 32, 2007).

4. S. Basnet *et al.*, Phys. Rev. C **100**, 065204 (2019), arXiv:1911.11681 [nucl-ex] .

5. D. Gaskell, T. Horn, and G. Huber, *Update on E12-06-101: Measurement of the Charged Pion Form Factor to High Q2 and E12-07-105: Scaling Study of the L-T Separated Pion Electroproduction Cross Section at 11 GeV*, Tech. Rep. (Jefferson Lab PAC 47 Jeopardy, 2019).

6. W. R. Frazer, Phys. Rev. **115**, 1763 (1959).

7. Horn, Tanja, EPJ Web Conf. **137**, 05005 (2017).

8. J. C. Collins, L. Frankfurt, and M. Strikman, Phys. Rev. D **56**, 2982 (1997), arXiv:hep-ph/9611433 .

9. T. Horn *et al.*, Phys. Rev. C **78**, 058201 (2008).

10. V. Barone and E. Predazzi, "Regge theory," in *High-Energy Particle Diffraction* (Springer Berlin Heidelberg, Berlin, Heidelberg, 2002) pp. 83–121.

11. J. Alcorn *et al.*, Nucl. Instrum. Meth. A **522**, 294 (2004).

12. Y. C. Chao, M. Drury, C. Hovater, A. Hutton, G. A. Krafft, M. Poelker, C. Reece, and M. Tiefenback, Journal of Physics: Conference Series **299**, 012015 (2011).

13. H. Fenker, *Hall C Document 808-v1: Hall C Experiment Readiness Review File 102*, Tech. Rep. (Hall C Jefferson Lab, 2016).

14. "Hall c 12 gev shms/hms experiments," (2017).

15. C. Yero, *Cross Section Measurements of Deuteron Electro-Disintegration at Very High Recoil Momenta and Large 4-Momentum Transfers* (Q^2), Ph.D. thesis, Florida Intl. U. (2020), arXiv:2009.11343 [nucl-ex] .

Appendices

A Elastic Calibration Write-Up

Energy Calibration of the NPS Calorimeter

Jacob Murphy
Ohio University

April 13, 2021

1 Introduction

Simulations of various elastic kinematics were completed in preparation for the DVCS experiment using the NPS calorimeter. Elastic calibration, where scattered electrons and recoiling protons are measured in coincidence, is required for every block of the calorimeter at various particle energies incoming on the blocks. The calibration makes it possible to establish the relationship between the FADC signal and the incoming particle energy. Our choice is to measure an elastically recoiling proton in the HMS in coincidence with the scattered electron in the NPS calorimeter (see Figure 1). In this configuration the precisely measured proton momentum and the knowledge of the beam energy can be used to predict the energy of the scattered electron. Due to the combined acceptance of both the HMS and the calorimeter, it is not guaranteed that coincidental elastic events can be recorded for every block of the calorimeter. Varying calorimeter angle and distance from the target allows for a greater acceptance for coincidence events. This study found that a calorimeter distance of 6 meters from the pivot point provides an apt balance between increasing the vertical coincidence acceptance and keeping a reasonable rate of events. At that distance, the calorimeter angle will need to be adjusted several times to calibrate all blocks; the number of adjustments, along with the rates, depends on the kinematics.

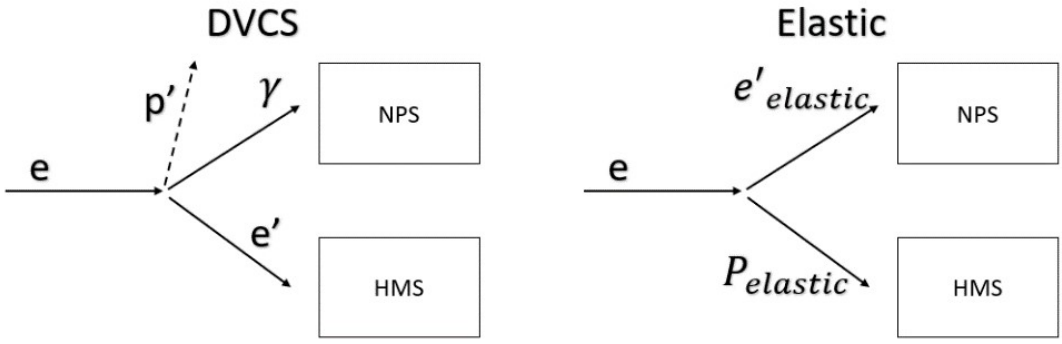

Fig. 1: Diagram of DVCS Experiment vs Elastic Calibration.

2 Experiment Set-Up

The target is liquid hydrogen, with density 0.07229 g/cm^3, and length of 10 cm. It is centered on a pivot point, where the detector distances are measured from; the target lies along the z-axis. The rest mass of the protons in the target is 0.938272 GeV/c^2. The electron beam travels along the z-axis and has energy values in the GeV range. The calorimeter is in the negative y-direction, or to the left of the beam-path viewed from above; this can be seen in Figure 2. It is on a track and can be placed between 3m and 11m from the pivot point. The angle of the calorimeter with respect to the beam-line can be adjusted from 6 degrees to 23 degrees. The face of the calorimeter is 65 cm wide by 74 cm tall, consisting of 1116 blocks.

The High Momentum Spectrometer, or HMS, in Hall C is in the positive y-direction, or to the right of the beam-path viewed from above. Again this can be seen in Figure 2. The collimator face is fixed at 1.6637 m from the pivot point. The angle of the HMS can be adjusted from 12.5 degrees to roughly 90 degrees. The collimator of the HMS is octagonal in shape, with a maximum width of 9.15 cm and a maximum height of 23.292 cm. It accepts momentum values ranging from 0.5 to 7.5 GeV. Above 5 GeV, however, the magnets of the HMS begin to saturate, though there has been data taken with the HMS up to 6.3 GeV. This will require extra calibration for both the DVCS experiment and the elastic calibrations. The momentum acceptance used for this simulation is ± 8%.

3 The Simulation

The simulation requires some input values to run – the beam energy and the detector positions. After these values are taken, three more are generated for each simulated event. First a vertex,

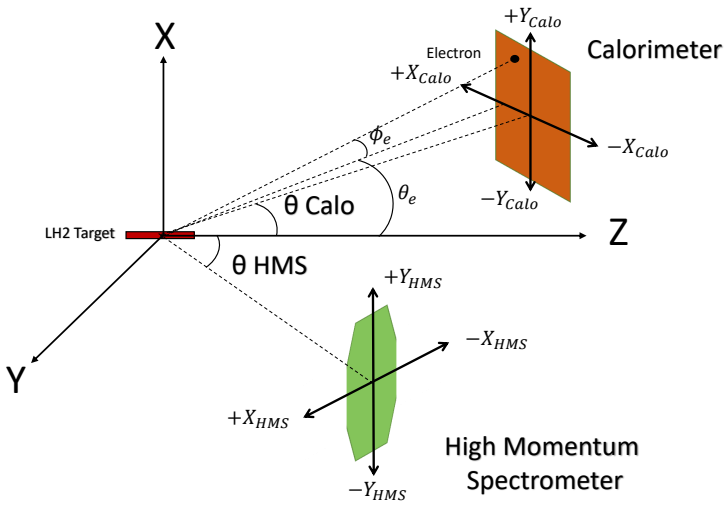

Fig. 2: Diagram of simulated experiment set-up, with axes. The origin is the pivot point centered on the LH2 target. The beam travels along in the positive Z-direction.

or scattering origin point, is randomly generated. The electrons in the beam may hit a proton anywhere along the target; given the target dimensions a vertex is chosen from -0.05m to 0.05m. Next, given the position of the calorimeter, a scattering angle for the electron is randomly generated. For a given position of the calorimeter (angle with respect to the beam line and distance to the target center) and a given length of the target, the minimum and maximum electron scattering angle resulting in a detection are computed. The electron scattering angle, see Figure 2, with respect to the beam-line, in the y-z plane (θ_e^C)[1] is generated to be within this region adding (subtracting) 1 degree on far (near) side of the detector face/entrance, where far (near) is referring to proximity to the beam line. Finally, the electron's out of plane scattering angle (ϕ^C) is generated within $\pm$ 7 degrees. This was chosen as it generates a solid angle covering the calorimeter face for any allowed distance from the center of the target to the calorimeter. Together, the horizontal and vertical angle ranges generate a solid angle over-encompassing the face of the calorimeter. These bounds are seen in Figure 3 in the top plots, as the black data points.

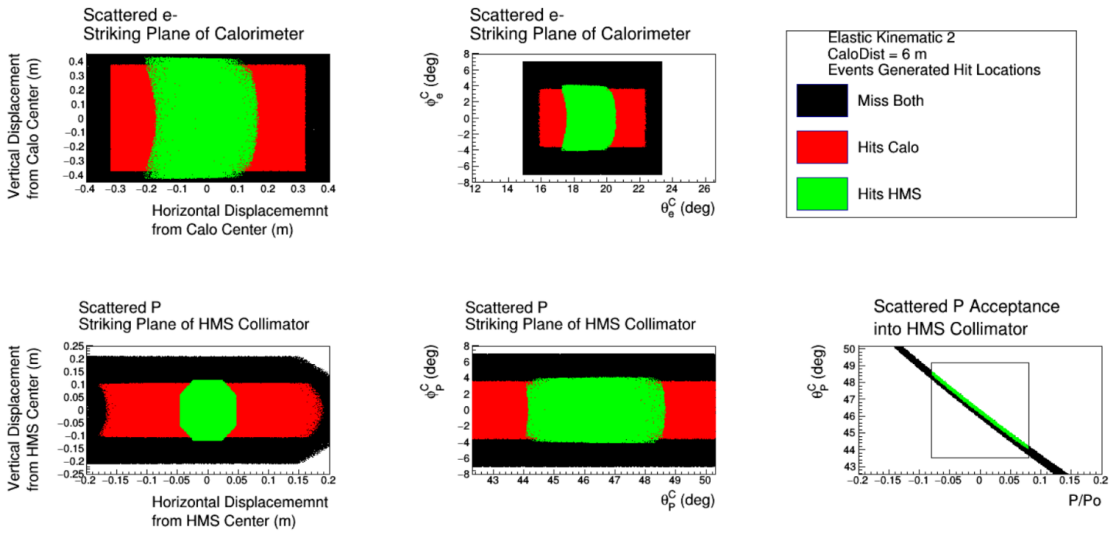

Fig. 3: Results of the simulation of elastic kinematic 2, at a calorimeter distance of 6 meters from the pivot point. The first subfigure shows electrons striking the plane of the face of the calorimeter. Similarly, the fourth shows where protons strike the plane of the collimator of the HMS. The second and fifth subfigures show the same results but with electron and proton angles (Cartesian). The sixth subfigure shows the limitations of the HMS acceptance, with the X-axis being normalized momentum and the y-axis being incoming θ^C angle.

As this is an elastic kinematic, the scattered momenta and angles of both particles are calculated from what has been determined so far. ϕ_P, the out-of-plane angle of the scattered proton is simply the opposite of ϕ_e, the out-of-plane angle of the scattered electron. θ_e, the spherical angle of the scattered proton, is then calculated using the beam energy and electron scattering angle.

$$\theta_P = atan(\frac{1}{(1 + k/m_p)tan(\theta_e/2)}) \tag{1}$$

[1] θ and ϕ are spherical angles while θ^C and ϕ^C are Cartesian angles.

Similarly, the momentum of the scattered proton and electron are determined.

$$k' = \frac{k}{1 + \frac{2k}{m_p} sin^2\theta_e/2} \tag{2}$$

$$P = \sqrt{(k + m_P - k')^2 - m_P^2} \tag{3}$$

From the trajectory of the scattered particles and their intercept with the planes at the face/entrance of the detectors, the simulation next checks to see if the particles hit the entrance face of their respective detectors. The first check in that regard is where the particles strike the plane of the detectors. This is done using the position of the detector, factoring in the offset from the vertex value, and using the difference in θ and ϕ angles between the detector and particle. For simplicity, the center of the detector face was set to be the origin of its own coordinate system. The vertical displacement is defined as positive upwards and negative downwards; the horizontal displacement is defined as positive away from the beam-line and negative towards the beam-line. Note that this results in mirrored coordinate systems between the calorimeter and HMS, where the former has a positive vertical displacement to the left while the latter has one to the right. If the particle position lands within the bounds of the detector's face, then it will hit the calorimeter. This is seen in Figure 3 as the red data points in the top figures. For the HMS, the simulation also checks for the scattered proton's momentum, as the HMS only has a $\pm$ 8% acceptance for its nominal momentum value. If the momentum falls within that range and lands within the entrance of the HMS, it is considered a 'hit'. The 'hit' region is seen in Figure 3 as the green data points in the bottom plots. Note that due to the additional constraint of the momentum acceptance, the region in green is less-defined than the red in sub-figures 1, 2, and 5. The last plot explicitly shows the $\pm$ 8% acceptance. The simulation generates 1 million events for a given kinematic, uniformly generating electron scattering angle and vertex for each event, then saves the results. The simulation was initially run for dozens of kinematic settings in addition to several calorimeter distances.

4 Rate Calculation

From these results, a separate script calculates the rate at which coincidence events occur. First the luminosity of the experiment is calculated for the liquid hydrogen target, assuming a beam current of 1 μA.

$$L = \frac{Q \times N_A \times \rho \times l}{e \times A_H} = 2.7 \times 10^{36} cm^{-2}/s \tag{4}$$

Where L is the luminosity of the experiments, Q is the charge (1 μA per second), N_A is Avagadro's number, ρ is the density of the hydrogen target (0.07229 g/cm^3), l is the length of the target (again, see Experiment Set-Up), e is the charge of the electron, and A_H is the molar mass of hydrogen in g/mol. Next, from the results of the simulation, an average $\frac{d\sigma}{d\Omega}$ is calculated from coincidence events. $d\Omega$ is found using

$$d\Omega = \Delta\theta\Delta\phi \times N_{Co}/N_G \tag{5}$$

where $\Delta\theta$ and $\Delta\phi$ are the range in Cartesian angles of the scattered electron allowed by the simulation. N_{Co}/N_G is the ratio of the number of coincidence events to the total number of events

generated. These three terms, luminosity, cross section, and solid angle, then result in a product which is the rate of coincidence events per second, R.

$$R = \frac{d\sigma}{d\Omega} \times d\Omega \times L \tag{6}$$

Following this, the rate of coincidence events per second per block, R_B, is then

$$R_B = \frac{R}{N_{Co}/N_{Calo} \times B} \tag{7}$$

where N_{Co}/N_{Calo} is the ratio of number of coincidence events to the number of events that have a calorimeter 'hit', and B is the number of calorimeter blocks, 1116.

5 Results

Variable	Units	Kin2	Kin6	Kin11
k	GeV	4.4	6.6	8.8
k'	GeV	3.5	5.5	7.5
θ_e	deg	19.1	13.7	11
P	GeV	1.58	1.81	2.03
θ_P	deg	46.3	46	44.9
Rate	Events/sec	87	64	45
Rate per Block	$\times 10^{-2}$ Events/sec	24	25	22
Time to 1000 Events per Block	hrs	1.2	1.1	1.3
% Calorimeter in Coincidence	%	30	21	17

Tab. 1: Proposed Elastic Kinematics, maximizing cross section while restricted by experimental bounds (see Experiment Set-Up). Angles are taken as absolute value in this study. Rate is calculated for 1 μA. The full height of the calorimeter is in coincidence with the HMS, seen by the green over-encompassing the red vertically. This ensures that, given multiple runs at varying angles, every block will eventually be in coincidence with the HMS. Note that the k' values do not match DVCS q' values exactly.

To reiterate, the goal of this simulation is to calibrate the calorimeter for NPS-DVCS. This will be done with elastically scattered electrons of energies comparable to those of the real photons of the NPS-DVCS kinematics, as seen in Tables 2 and 3. Therefore, when simulating kinematics for calibration, the scattered electron energy is constrained by what is needed for the NPS-DVCS kinematics. There are two other major constraints on the simulation: ensuring every calorimeter block is calibrated and minimizing data-taking time.

To calibrate every block, the distance from the calorimeter to the target must be large enough such that the vertical extension of the calorimeter face is covered by coincidence events. As seen in Figure 5, it was found that this occurs at approximately a 6 meter distance from the target to the calorimeter. This result is independent of the kinematics. While the entirety of the calorimeter is not struck by coincidence events in this kinematic, full horizontal coverage is achievable by repeated runs at varying calorimeter angles. Note that further increasing the calorimeter's distance to the target will increase the horizontal coverage, but at the cost of increasing events missed in the vertical. This leads to an overall decrease in event-rate which increases data-taking time (see section 4).

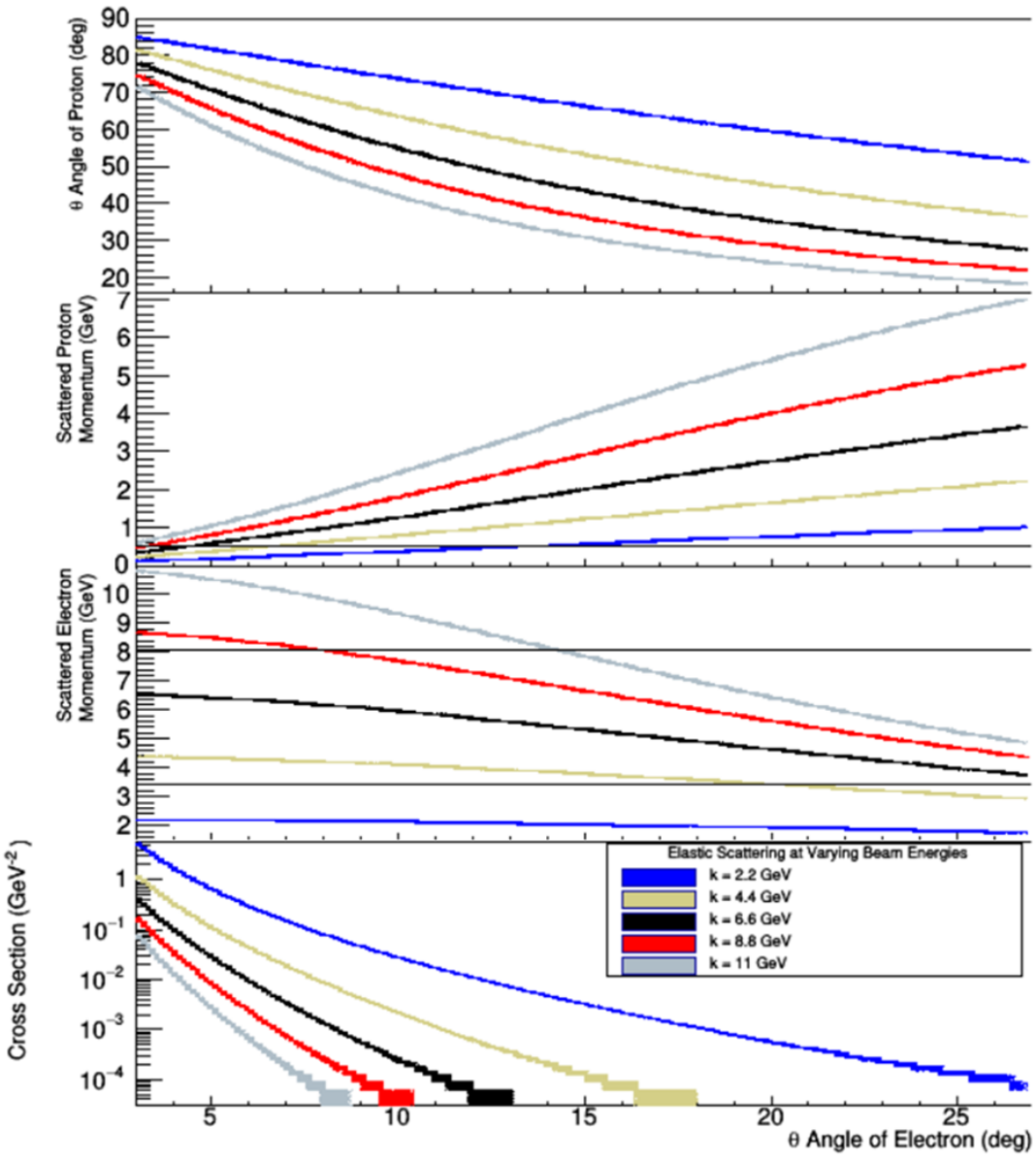

Fig. 4: Plots of scattered electron θ angle varying beam energy. The subplots show from top to bottom, proton scattering angle θ, scattered proton momentum, scattered electron momentum, and cross section. In the second subplot, the black horizontal line shows the lower limit of the HMS nominal momentum, 0.5 GeV. In the third subplot, the black horizontal lines show the range of scattered photon energies expected for NPS-DVCS: 3.4 to 8.1 GeV (see Tables 2 and 3)

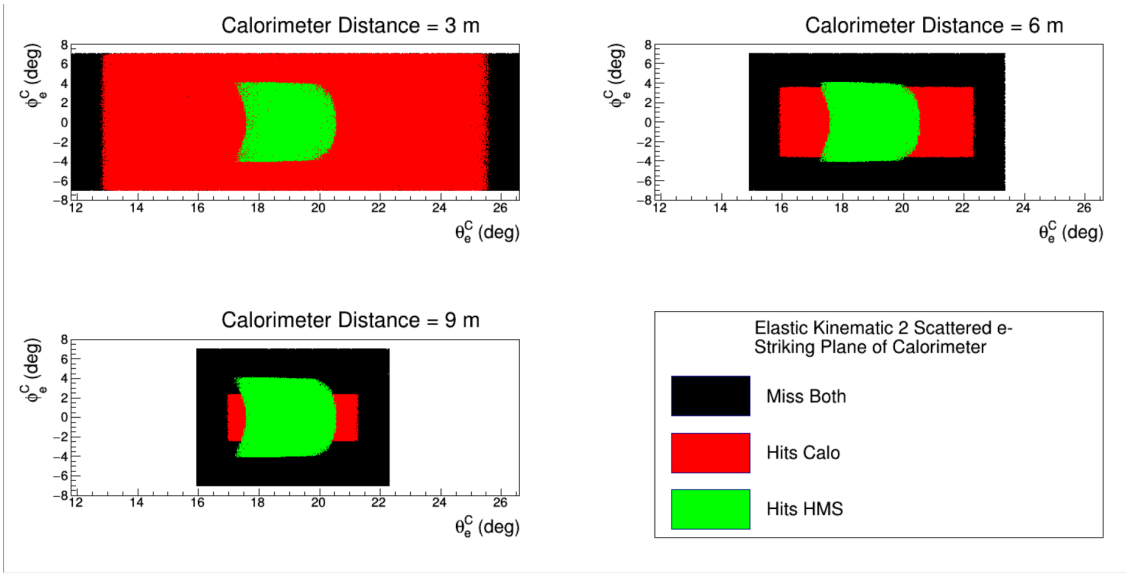

Fig. 5: Results of the simulation of elastic kinematic 2, varying distance from the calorimeter to the target center. The figures show electrons striking the plane of the face of the calorimeter, with the axes plotting θ_e^C vs ϕ_e^C.

To minimize data-taking time, the cross section must be maximized. The relationship between cross section and other factors in the simulation can be seen in Figure 4. Decreasing beam energy and θ_e will drastically increase the cross section. However, the goal is still to collect scattered electrons of specific energy levels. As such, for a given scattered electron energy, the beam energy must always be greater.

Considering these constraints and limitations, fourteen kinematics were simulated and their rates calculated, with the distance from the calorimeter to the target fixed at 6 meters [2]. These kinematics are seen in Tables 4 and 5. The scattered electron momenta span a range similar to the NPS-DVCS photons, but using the lowest possible beam energy[3]. A kinematic was studied for every 0.5 GeV from 3 to 8.5 GeV, cycling through the entire range of scattered photon momenta expected in the NPS-DVCS experiment. There were three immediate issues with these elastic kinematics: the momenta of the elastic proton collected by the HMS, the required angle of the calorimeter for collecting the scattered electron, and the coincidence event rate. Because beam energy was minimized, the energy of the scattered electrons approaches the beam energy in some of the kinematics. As this happens, the scattered momentum of the proton can fall below what the HMS can collect and the angle of the scattered electron can become too small for the calorimeter to reach. On the other hand, the larger the difference between the beam energy and scattered electron momentum, the cross section (and proportionally the event rate) drops off. Also with this, the calorimeter angle increases, sometimes beyond what the calorimeter can reach (see 2). These relationships can be seen in Figure 4. Considering these limitations, many kinematics were not simulated. The ones removed from consideration had either θ_e outside the bounds of the

[2]These kinematics differ from those presented at the February 2020 NPS meeting. The previous kinematics used the NPS-DVCS k and q' values as their k and k' values (see Table 2) Kinematics discussed here share only the same range of energy values for k' with the NPS-DVCS q' values (see Tables 4 and 5).

[3]Kinematics here use the nominal beam energy. These values will be adjusted closer to the experiment.

calorimeter, scattered momenta of the proton below what the HMS can receive, or smaller cross sections (any cross section resulting in a coincidence event rate per block less than 0.1 Events/sec). This left 3 kinematics (Kine 2, 6, 11), as seen in Table 1. These kinematics were simulated using the aforementioned script.

The rates were calculated assuming a beam current of 1 μA, and examining the time to achieve 1000 events per block. Table 1 shows that this is achievable for all 3 kinematics in just over an hour. A restriction of this, however, is that the entirety of the calorimeter cannot be covered at once, see Figure 5. Using the percentage of the calorimeter covered by coincidence events, we can assume 4 to 6 runs, with calorimeter angle adjustments between, will be required to fully calibrate. The number of adjustments can by reduced by moving the calorimeter further from the pivot point, but at the cost of increased data-taking time. If the distance is increased from 6 to 11 meters, for example, the percentage of the calorimeter covered roughly doubles while the time to 1000 coincidence events approximately quadruples.

6 Conclusion

From this simulation, it was found that full coverage of the calorimeter by elastic coincidence events is achievable by adjusting the calorimeter distance to be 6 meters from the pivot point, then adjusting calorimeter angle for multiple runs to cover the horizontal spread of its face. This will allow every calorimeter block to be calibrated by elastic events. Fixing the calorimeter distance, 14 kinematics were examined. From these, three were found to be possible given the experiment's limitations, which were then simulated. These kinematics, labeled 2, 6, and 11, range in scattered electron momentum by 3.5, 5.5, and 7.5 GeV. At 1 μA beam current, each of these kinematics simulated were found to achieve 1000 coincidence events per block in just over an hour. A higher beam current or lower coincidence event threshold will decrease this time further. Given the percentage of the calorimeter face covered by coincidence events, each calibration will need to be run 4 to 6 times, adjusting calorimeter angle to sweep its face horizontally.

7 Appendix

Variable	Energy Dependence at fixed (Q^2,x_B)												Low-x_B				High-Q^2
x_B	0.36					0.5			0.60				0.2				0.36
Q^2 (GeV^2)	3.0			4.0		3.4		4.8	5.1			3.0	2.0			3.0	5.5
k (GeV)	6.6	8.8	11	8.8	11	8.8	11	11	6.6	8.8	11	11	6.6	8.8	11	11	11
k' (GeV)	2.2	4.4	6.6	2.9	5.1	5.2	7.4	5.9	2.1	4.3	6.5	5.7	1.3	3.5	5.7	3.0	2.9
q' (GeV)	4.4	4.4	4.4	5.8	5.8	3.4	3.4	4.9	4.2	4.2	4.2	5.0	5.3	5.3	5.3	8.0	8.1

Tab. 2: Approved PAC 40 DVCS and π0 kinematics for Hall C.

Variable	Jeopardy Kinematics			
x_B	0.480	0.600		
Q^2 (GeV^2)	5.334	6.822		8.40
k (GeV)	10.617	8.517	10.617	8.517
k' (GeV)	4.696	2.458	4.558	1.057
q' (GeV)	5.736	5.697	5.697	7.089

Tab. 3: PAC 47 DVCS jeopardy kinematics for Hall C.

Variable	Kine1	Kine2	Kine3	Kine4	Kine5	Kine6	Kine7
k (GeV)	4.4	4.4	4.4	6.6	6.6	6.6	6.6
k' (GeV)	3	3.5	4	4.5	5	5.5	6
θ_e (deg)	25.8	19.1	11.85	20.99	17.3	13.7	9.7
θ_P (deg)	37.5	46.3	59.43	33.9	39.2	46	55.8
P (GeV)	2.14	1.58	0.9543	2.89	2.35	1.81	1.22
$\theta_e + \theta_p$ (deg)	63.3	65.4	71.28	54.89	56.5	59.7	65.5
Rate (Events/sec)	2.7	87	2082	2.9	11	64	791
Rate per Block ($\times 10^{-2}$ Events/sec)	2.1	24	870	0.67	3.3	25	420
Time to 1000 Events per Block (hrs)	13	1.2	0.032	41.7	8.2	1.1	0.066
% Calorimeter in Coincidence	42.50	30.00	20.00	36.00	28.00	21.00	15.00

Tab. 4: Potential Elastic Kinematics, arranged in increasing k'

Variable	Kine8	Kine9	Kine10	Kine11	Kine12	Kine13	Kine14
k (GeV)	6.6	8.8	8.8	8.8	8.8	8.8	11
k' (GeV)	6.5	6.5	7	7.5	8	8.5	8.5
θ_e (deg)	3.8	15.79	12.4	11	8.37	5	12.86
θ_P (deg)	75.1	34.79	39.3	44.9	52.8	65.7	34.89
P (GeV)	0.44	3.1	2.57	2.03	1.46	0.81	3.308
$\theta_e + \theta_p$ (deg)	78.9	50.58	51.7	55.9	61.17	70.7	47.75
Rate (Events/sec)	74500	2.9	10	45	374	13000	2.7
Rate per Block ($\times 10^{-2}$ Events/sec)	102000	0.92	3.9	22	233	11100	1.1
Time to 1000 Events per Block (hrs)	0	30.2	7.2	1.3	0.12	0.0025	26.1
% Calorimeter in Coincidence	4.00	26.00	21.00	17.00	13.00	9.00	21.00

Tab. 5: Potential Elastic Kinematics, arranged in increasing k'

B Machine Learning Write-Up

ML Challenge 6

Jacob Murphy, Julie Roche
Ohio University Physics and Astronomy Department

August 2020

1 Introduction

The calorimeter used for DVCS in Hall A consists of an assembly of 13x16 lead-glass blocks. Each block reads out a voltage signal produced as a result of an initial photon hitting the block; it is sampled every 1 ns and stored into a 128 integer array. The shape-versus-time of the signal produced by a block is a characteristic of the lead-block material and is well known. Using this, a recursive two steps analysis system based on χ^2 minimization is used in understanding the precise time of arrival of the high energy photon (better than 1 ns) as well as its total energy (better than 2%). The arrival time (t_0) of the signal and the overall amplitude (A) vary event per event. Figure 1 shows a large single pulse measured by a block. For most events, only one high energy photon hits the calorimeter at the time. Complications to this analysis scheme arise from the events for which multiple photons hit the calorimeter within the 128 ns time frame, as seen in Figure 2.

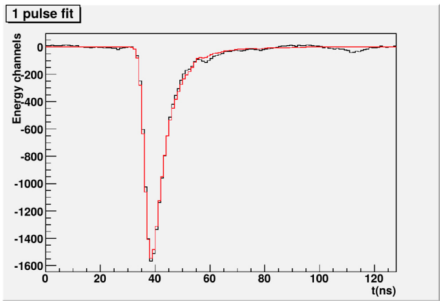

Fig. 1: Clean large signal from a block. The black points are the data while the red trace is the offline fitted signal.

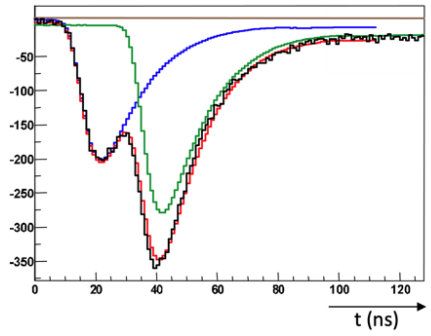

Fig. 2: Typical two pulse signal. The data are the black line. The total fitted signal is in red and is the sum of two pulses of different amplitudes A arriving at different times (blue 20ns and green 40ns).

2 Goal

The goal is to design and train a model such that given an input of 128 signals, can output the amplitude and arrival time of any potential pulses. The maximum possible number of pulses is 2, meaning this output consists of 4 values: A1, A2, t1, t2. Where A is the amplitude of a pulse and t is the arrival time of the pulse, or time of the peak.

Amplitude is always taken as a positive value for real data. For example, an Amplitude of 400 would mean a peak going down to -400 Energy Channels. Arrival time is the time to the pulse peak since the start of the signal. The first signal is at time 0 ns, and the last is at time 127 ns. Should a pulse be non-existent, its amplitude should output as 0 and arrival time as -1. The definition of pulse 1 vs pulse 2 is not a priority

for this problem, so pulse 1 may have the larger arrival time and bigger or smaller amplitude, and pulse 2 could be the only pulse in the array of signals.

The model will be expected to accept a 128-signal input and always output the 4 values A1, A2, t1, and t2. The size of the input will not vary, though the number of pulses in the input will be either 0, 1, or 2. The model should be able to recognize how many pulses there are and return 0 amplitude and -1 arrival time for non-existent pulses. In other words, a 0-pulse event should output A1 = A2 = 0, and t1 = t2 = -1. A 1-pulse event should output either A1 = 0 and t1 = -1 or A2 = 0 and t2 = -1.

3 Materials

All materials are available **here**. Individual copies can be made available by emailing Jacob Murphy at jm443918@ohio.edu.

The training set will consist of rows of 133 comma-separated values. The first 5 are the baseline value, A1, A2, t1, t2. The baseline value is the average value of the signal without pulses. It is not required to be found but rather given to potentially help with training. The remaining 128 values are the signal values from time 0 ns to time 127 ns. The training set contains a little over 190k events.

The test set will be a CSV file with only the 128 signal inputs. Aside from missing the first 5 values, the format will be identical to the training set. Output is expected to be of a similar form to the training set: a CSV file with 4 columns (A1, A2, t1, t2) and a row for every event.

4 Judging Criteria

On Wednesday, November 4th at noon, the test set will be released. Participants will have 48 hours, or until Friday, November 6th at noon, to make a submission. Submissions should be sent to Jacob Murphy at jm443918@ohio.edu and must consist of all scripts used for training and testing, along with the results from the test set in a CSV file. The results should contain a row for every event and 4 columns for A1, A2, t1, and t2 (in that order). Any submission not based on ML only will be disqualified (eg. no pre-processing with traditional methods). There are no restrictions for ML methods.

For each value (A1, A2, t1, t2), the submission will be compared to the true values (those found with traditional methods) and the sum of the difference squared will be taken. For these values, each pulse will be compared to both true pulse values and the lower difference will be taken. In other words, if the submitted pulse 1 matches better with the true pulse 2, that difference will be used for the sum. Similarly, the number of pulses found will be compared to the true value and the sum of the difference squared will be taken. Number of pulses will be determined by non-zero amplitudes in conjunction with corresponding time values not equal to -1.

The individuals or teams with the lowest sum in each of the 5 categories (A1, A2, t1, t2, pulse number) will receive 3 points. The next lowest in each category will receive 2, and then 1. Ties in these categories will receive equal points, with the next rank being skipped (ie two 1st places followed by 3rd, or two 2nd places followed by no score). The highest total score will win, with ties being broken by the scores for pulse number.